The Astrophysical Journal, 979:123 (11pp), 2025 February 1 https://doi.org/10.3847/1538-4357/ada352

The Microlensing Event Rate and Optical Depth from MOA-II 9 Yr Survey Toward the Galactic Bulge

Kansuke Nunota[1], Takahiro Sumi[1], Naoki Koshimoto[1], Nicholas J. Rattenbury[2], Fumio Abe[3], Richard Barry[4], David P. Bennett[4,5], Aparna Bhattacharya[4,5], Akihiko Fukui[6,7], Ryusei Hamada[1], Shunya Hamada[1], Naoto Hamasaki[1], Yuki Hirao[8], Stela Ishitani Silva[4,9], Yoshitaka Itow[3], Yutaka Matsubara[3], Shota Miyazaki[10], Yasushi Muraki[3], Tsutsumi Nagai[1], Greg Olmschenk[4], Clement Ranc[11], Yuki K. Satoh[12], Daisuke Suzuki[1], Paul. J. Tristram[13], Aikaterini Vandorou[4,5], and Hibiki Yama[1]
(MOA collaboration)
[1] Department of Earth and Space Science, Graduate School of Science, Osaka University, Toyonaka, Osaka 560-0043, Japan
[2] Department of Physics, University of Auckland, Private Bag 92019, Auckland, New Zealand
[3] Institute for Space-Earth Environmental Research, Nagoya University, Nagoya 464-8601, Japan
[4] Code 667, NASA Goddard Space Flight Center, Greenbelt, MD 20771, USA
[5] Department of Astronomy, University of Maryland, College Park, MD 20742, USA
[6] Department of Earth and Planetary Science, Graduate School of Science, The University of Tokyo, 7-3-1 Hongo, Bunkyo-ku, Tokyo 113-0033, Japan
[7] Instituto de Astrofisica de Canarias, Via Lactea s/n, E-38205 La Laguna, Tenerife, Spain
[8] Institute of Astronomy, Graduate School of Science, The University of Tokyo, 2-21-1 Osawa, Mitaka, Tokyo 181-0015, Japan
[9] Department of Physics, The Catholic University of America, Washington, DC 20064, USA
[10] Institute of Space and Astronautical Science, Japan Aerospace Exploration Agency, 3-1-1 Yoshinodai, Chuo, Sagamihara, Kanagawa 252-5210, Japan
[11] Sorbonne Université, CNRS, UMR 7095, Institut d'Astrophysique de Paris, 98 bis bd Arago, 75014 Paris, France
[12] College of Science and Engineering, Kanto Gakuin University, 1-50-1 Mutsuurahigashi, Kanazawa-ku, Yokohama, Kanagawa 236-8501, Japan
[13] University of Canterbury Mt., John Observatory, P.O. Box 56, Lake Tekapo 8770, New Zealand
Received 2024 October 29; revised 2024 December 5; accepted 2024 December 9; published 2025 January 22

Abstract

We present measurements of the microlensing optical depth and event rate toward the Galactic bulge using the data set from the 2006 to 2014 MOA-II survey, which covers 22 bulge fields spanning $\sim 42\,\mathrm{deg}^2$ between $-5^\circ < l < 10^\circ$ and $-7^\circ < b < -1^\circ$. In the central region with $|l| < 5^\circ$, we estimate an optical depth of $\tau = [1.75 \pm 0.04] \times 10^{-6} \exp[(0.34 \pm 0.02)(3^\circ - |b|)]$ and an event rate of $\Gamma = [16.08 \pm 0.28] \times 10^{-6} \exp[(0.44 \pm 0.02)(3^\circ - |b|)]\,\mathrm{star}^{-1}\,\mathrm{yr}^{-1}$ using a sample consisting of 3525 microlensing events, with Einstein radius crossing times of $t_\mathrm{E} < 760$ days and a source star magnitude of $I_\mathrm{s} < 21.4$ mag. We confirm our results are consistent with the latest measurements from the OGLE-IV 8 yr data set. We find our result is inconsistent with a prediction based on Galactic models, especially in the central region with $|b| < 3^\circ$. These results can be used to improve the Galactic bulge model, and more central regions can be further elucidated by upcoming microlensing experiments, such as the PRime-focus Infrared Microlensing Experiment and Nancy Grace Roman Space Telescope.

Unified Astronomy Thesaurus concepts: Galactic center (565); Milky Way Galaxy (1054); Microlensing event rate (2146); Microlensing optical depth (2145); Gravitational microlensing (672)

Materials only available in the online version of record: machine-readable table

1. Introduction

Gravitational microlensing provides a powerful method to probe the structure, kinematics, and dynamics of our Galaxy by measuring the event rate and optical depth. These measurements are directly connected to the mass, velocity, and density distributions of the Galaxy (K. Griest et al. 1991; B. Paczynski 1991). Through microlensing surveys, we gain valuable insights into Galactic properties and the distribution of matter, including dark matter.

Currently, several groups—Microlensing Observations in Astrophysics (MOA-II[14]; I. A. Bond et al. 2001; T. Sumi et al. 2003), the Optical Gravitational Lensing Experiment (OGLE-IV[15]; A. Udalski et al. 2015), and the Korea Microlensing Telescope Network (KMTNet[16]; S.-L. Kim et al. 2016)—are conducting microlensing surveys toward the Galactic bulge (GB) and detect a couple of thousand microlensing events every year.

Historically, the first measurements of microlensing optical depth toward the GB revealed significant discrepancies between observed values and theoretical predictions. Early studies, such as A. Udalski et al. (1994) and C. Alcock et al. (1997), reported optical depths that exceeded predictions by a factor of several, prompting discussions on the potential role of Galactic bars and other systematic biases. Subsequent works refined these measurements by focusing on well-characterized source stars, such as red clump giants (RCGs; C. Afonso et al. 2003; P. Popowski et al. 2005; C. Hamadache et al. 2006), leading to revised, but still elevated, optical depth estimates.

[14] https://www.massey.ac.nz/ iabond/moa/alert2024/alert.php

[15] https://ogle.astrouw.edu.pl/ogle4/ews/ews.html
[16] https://kmtnet.kasi.re.kr/ulens/

In recent years, T. Sumi et al. (2013) and T. Sumi & M. T. Penny (2016) analyzed data from two years of the MOA-II survey during 2006–2007, providing optical depth estimates corrected for incompleteness in source star counts. Similarly, P. Mróz et al. (2019) used the data from the OGLE-IV survey spanning 2010–2017 to measure microlensing optical depths, reporting values approximately 30% lower than those from MOA-II. This discrepancy may arise from differences in the assumed number of source stars in the respective analyses. These studies highlight the importance of accurate source star counts in deriving microlensing optical depths.

Despite these efforts, discrepancies persist between measurements from different surveys, alongside uncertainties in the completeness and potential systematic biases of source star counts. In particular, the discrepancy between the independent measurements from T. Sumi & M. T. Penny (2016) and P. Mróz et al. (2019) calls for further investigation. To resolve this, it is essential to update the MOA-II measurements with a more comprehensive data set. Such updates not only contribute to resolving discrepancies between the MOA and OGLE measurements but also provide independent observational constraints, distinct from those in P. Mróz et al. (2019), which can be utilized to further refine and validate current Galactic models.

In this study, we present a new measurement of the microlensing optical depth and event rate toward the GB, utilizing the data set from N. Koshimoto et al. (2023). This work aims to address the incompleteness and systematic biases identified in previous studies, providing updated and independent observational constraints.

The structure of this paper is as follows. Section 2 introduces the formalism used to calculate the microlensing optical depth and event rate. Section 3 describes our data and the selection criteria for microlensing events. In Section 4, we present our results for the microlensing optical depth and event rate. Section 5 compares our findings with previous studies and theoretical predictions. Finally, Section 6 summarizes our conclusions.

2. Formalism

Gravitational microlensing occurs when the gravitational field of a foreground object acts as a lens, bending the light from a more distant background source. The magnification of a background source is given by B. Paczynski (1986)

$$A(u) = \frac{u^2 + 2}{u\sqrt{u^2 + 4}}, \tag{1}$$

where u is the angular separation of the source and lens scaled by the angular Einstein radius, $\theta_{\rm E}$, which is given by

$$\theta_{\rm E} = \sqrt{\frac{4G}{c^2} M_{\rm L}\left(\frac{1}{D_{\rm L}} - \frac{1}{D_{\rm S}}\right)}, \tag{2}$$

where $D_{\rm L}$ and $D_{\rm S}$ are distance to the lens and source, respectively, and $M_{\rm L}$ is the lens mass, G is the gravitational constant, and c is the speed of light. u can be written as a function of time

$$u(t) = \sqrt{u_0^2 + \left(\frac{t - t_0}{t_{\rm E}}\right)^2}, \tag{3}$$

where u_0, t_0, and $t_{\rm E}$ are the minimum impact parameter, the time of maximum magnification, and the Einstein radius crossing time, respectively. The Einstein radius crossing time, $t_{\rm E}$, is given by $t_{\rm E} = \theta_{\rm E}/\mu_{\rm rel}$, where the lens-source relative proper motion $\mu_{\rm rel}$ is given by $\mu_{\rm rel} = |\boldsymbol{\mu}_{\rm L} - \boldsymbol{\mu}_{\rm S}|$, where $\boldsymbol{\mu}_{\rm L}$ is the lens proper motion vector and $\boldsymbol{\mu}_{\rm S}$ is the source proper motion vector.

The microlensing optical depth, τ, is defined as the probability that a given star is inside the Einstein ring of a lens at any given time. The probability that one source at distance, $D_{\rm S}$, is inside the Einstein ring, $\tau(D_{\rm S})$, is given by

$$\begin{aligned}\tau(D_{\rm S}) &= \int_0^{D_{\rm S}} \left[\int n(M_{\rm L}, D_{\rm L}) \pi R_{\rm E}^2(M_{\rm L}, D_{\rm L}) dM_{\rm L}\right] dD_{\rm L} \\ &= \pi \frac{4G}{c^2} \int_0^{D_{\rm S}} \rho(D_{\rm L}) D_{\rm L}\left(1 - \frac{D_{\rm L}}{D_{\rm S}}\right) dD_{\rm L},\end{aligned} \tag{4}$$

where $n(M_{\rm L}, D_{\rm L})$ is the number density of lenses with the mass, $M_{\rm L}$, at the distance, $D_{\rm L}$, $R_{\rm E} = D_{\rm L}\theta_{\rm E}$ is the Einstein radius, and $\rho(D_{\rm L}) = \int M_{\rm L} n(M_{\rm L}, D_{\rm L}) dM_{\rm L}$ is the mass density of lenses. The observable quantity is just the integrated optical depth averaged over all detectable source stars toward the line of sight i.e.,

$$\tau = \frac{1}{N_{\rm s}} \int_0^{\infty} \tau(D_{\rm S}) N(D_{\rm S}) dD_{\rm S} \tag{5}$$

where $N(D_{\rm S})$ is the number density of source stars at distance, $D_{\rm S}$, and $N_{\rm s} = \int_0^{\infty} N(D_{\rm S}) dD_{\rm S}$ is the number of all detectable source stars in the direction of sight.

The microlensing event rate is defined as the probability of an occurrence of a microlensing event per source star per unit time. The area swept per unit time by the Einstein ring of a lens with mass, $M_{\rm L}$, and projected relative velocity $v_{\rm rel}$ at a distance $D_{\rm L}$ is given by $S(M_{\rm L}, D_{\rm L}, v_{\rm rel}) = 2v_{\rm rel} R_{\rm E}(M_{\rm L}, D_{\rm L}) \quad (= 2D_{\rm L}^2 \mu_{\rm rel} \theta_{\rm E}(M_{\rm L}, D_{\rm L}))$ (V. Batista et al. 2011). The probability that one source at distance, $D_{\rm S}$, is microlensed in unit time, γ, can be calculated by integrating $S(M_{\rm L}, D_{\rm L}, v_{\rm rel})$, i.e.,

$$\begin{aligned}\gamma(D_{\rm S}) = \int_0^{D_{\rm S}} dD_{\rm L} \int_0^{\infty} dM_{\rm L} \int_0^{\infty} \\ \times d\mu_{\rm rel} \quad S(M_{\rm L}, D_{\rm L}, \mu_{\rm rel}) n(M_{\rm L}, D_{\rm L}, \mu_{\rm rel}),\end{aligned} \tag{6}$$

where $n(M_{\rm L}, D_{\rm L}, \mu_{\rm rel})$ is the local number density of lenses with mass, $M_{\rm L}$, and relative proper motion, $\mu_{\rm rel}$, at distance, $D_{\rm L}$. The microlensing event rate, Γ, is given by integration of $\gamma(D_{\rm S})$ with the number density of source stars, $N(D_{\rm S})$, i.e.,

$$\Gamma = \frac{1}{N_{\rm s}} \int_0^{\infty} \gamma(D_{\rm S}) N(D_{\rm S}) dD_{\rm S}. \tag{7}$$

Observationally, the microlensing optical depth can be expressed as the average ratio of the time when the source is within the Einstein radius to the duration of the survey. For each microlensing event, the time that the source star is within the Einstein radius is given by $2t_{\rm E}\sqrt{1 - u_0^2}$; however, since the distribution of u_0 is uniform between $0 \leqslant u_0 \leqslant 1$, we can calculate the average time that the source remains within the Einstein radius, which is given by $(\pi/2)t_{\rm E}$. Thus, we obtain the expression for τ as (A. Udalski et al. 1994)

$$\tau = \frac{\pi}{2N_{\rm s}T_{\rm o}} \sum_{i=1}^{N_{\rm eve}} \frac{t_{\rm E,i}}{\epsilon(t_{\rm E,i})}, \tag{8}$$

where $N_{\rm eve}$ is the number of observed events, $t_{\rm E,i}$ is Einstein radius crossing time of the ith event, $\epsilon(t_{\rm E,i})$ is the detection efficiency, $N_{\rm s}$ is the total number of monitored source stars, and $T_{\rm o}$ is the duration of the survey.

Table 1

MOA-II Galactic Bulge Fields with Galactic Coordinates of the Mean Field Center ($\langle l \rangle$,$\langle b \rangle$), the Number of Subfields Used ($N_{\rm sub}$), the Number of Source Stars ($N_{\rm s}$), the Number of Microlensing Events ($N_{\rm eve}$), the Microlensing Event Rate per Star per Year (Γ), the Microlensing Event Rate per Square Degree per Year ($\Gamma_{\rm deg^2}$), the Optical Depth (τ), and the Average Einstein Radius Crossing Time $\langle t_{\rm E} \rangle$

Field	$\langle l \rangle$ (°)	$\langle b \rangle$ (°)	$N_{\rm sub}$	$N_{\rm s}$	$N_{\rm eve}$	τ (10^{-6})	Γ (10^{-6} star^{-1} yr^{-1})	$\Gamma_{\rm deg^2}$ (deg^{-2} yr^{-1})	$\langle t_{\rm E} \rangle$ (days)
gb1	−4.33	−3.11	79	21047010	193	$1.68^{+0.15}_{-0.15}$	$12.86^{+0.27}_{-0.27}$	$125.73^{+2.69}_{-2.65}$	29.47 ± 1.12
gb2	−3.86	−4.39	79	17647488	133	$1.23^{+0.14}_{-0.13}$	$8.94^{+0.25}_{-0.25}$	$73.33^{+2.06}_{-2.02}$	31.22 ± 1.30
gb3	−2.35	−3.51	79	22711037	193	$1.38^{+0.13}_{-0.11}$	$11.30^{+0.25}_{-0.24}$	$119.20^{+2.62}_{-2.58}$	27.53 ± 1.03
gb4	−0.83	−2.63	77	25985143	307	$1.98^{+0.15}_{-0.14}$	$20.46^{+0.31}_{-0.31}$	$253.43^{+3.85}_{-3.81}$	21.91 ± 0.70
gb5	0.65	−1.86	65	29137851	492	$3.44^{+0.22}_{-0.21}$	$31.43^{+0.36}_{-0.36}$	$516.98^{+5.98}_{-5.94}$	24.77 ± 0.77
gb7	−1.72	−4.60	78	16344845	99	$0.81^{+0.09}_{-0.08}$	$7.91^{+0.25}_{-0.24}$	$60.86^{+1.89}_{-1.85}$	23.18 ± 0.83
gb8	−0.19	−3.75	78	22263658	186	$1.37^{+0.14}_{-0.12}$	$12.73^{+0.27}_{-0.26}$	$133.39^{+2.78}_{-2.74}$	24.39 ± 1.05
gb9	1.33	−2.88	79	33308780	466	$2.19^{+0.14}_{-0.13}$	$21.63^{+0.28}_{-0.28}$	$334.69^{+4.37}_{-4.33}$	22.86 ± 0.67
gb10	2.84	−2.09	70	21465124	282	$2.56^{+0.28}_{-0.26}$	$22.81^{+0.36}_{-0.36}$	$256.71^{+4.07}_{-4.03}$	25.35 ± 1.39
gb11	−1.11	−5.73	76	10931979	46	$0.59^{+0.11}_{-0.10}$	$4.80^{+0.24}_{-0.23}$	$25.33^{+1.24}_{-1.20}$	28.02 ± 2.04
gb12	0.44	−4.87	79	16090446	86	$0.79^{+0.10}_{-0.10}$	$7.06^{+0.23}_{-0.23}$	$52.76^{+1.75}_{-1.71}$	25.46 ± 1.20
gb13	1.97	−4.02	79	23728248	188	$1.32^{+0.13}_{-0.11}$	$11.03^{+0.24}_{-0.24}$	$121.53^{+2.64}_{-2.60}$	27.08 ± 1.08
gb14	3.51	−3.17	79	25094851	254	$1.58^{+0.14}_{-0.13}$	$14.33^{+0.27}_{-0.26}$	$166.99^{+3.09}_{-3.05}$	24.95 ± 0.90
gb15	4.99	−2.45	62	10404096	82	$1.86^{+0.29}_{-0.25}$	$13.02^{+0.39}_{-0.39}$	$80.18^{+2.43}_{-2.38}$	32.34 ± 2.04
gb16	2.60	−5.17	79	15028199	99	$1.17^{+0.17}_{-0.16}$	$7.38^{+0.25}_{-0.24}$	$51.49^{+1.73}_{-1.69}$	35.81 ± 2.28
gb17	4.15	−4.34	79	17979175	138	$1.09^{+0.11}_{-0.11}$	$9.37^{+0.25}_{-0.25}$	$78.28^{+2.12}_{-2.09}$	26.20 ± 0.97
gb18	5.69	−3.51	78	15478756	104	$1.27^{+0.17}_{-0.15}$	$8.56^{+0.26}_{-0.26}$	$62.37^{+1.91}_{-1.87}$	33.50 ± 1.81
gb19	6.54	−4.57	78	12087586	81	$1.15^{+0.16}_{-0.14}$	$7.48^{+0.28}_{-0.27}$	$42.56^{+1.58}_{-1.54}$	34.81 ± 1.95
gb20	8.10	−3.75	79	10730219	65	$1.19^{+0.21}_{-0.17}$	$7.25^{+0.29}_{-0.28}$	$36.14^{+1.45}_{-1.41}$	37.27 ± 2.56
gb21	9.60	−2.94	73	8321495	31	$0.70^{+0.16}_{-0.14}$	$4.87^{+0.27}_{-0.26}$	$20.36^{+1.14}_{-1.10}$	32.68 ± 2.79
all	1.85	−3.69	1536	378451020	3525	$1.61^{+0.04}_{-0.04}$	$14.00^{+0.07}_{-0.07}$	$126.60^{+0.61}_{-0.61}$	26.06 ± 0.27

Introducing $t_{\rm in} = (\pi/2)t_{\rm E}$ as the average time that a source remains within the Einstein radius, we can reinterpret part of Equation (8). Specifically, the term $\frac{\pi}{2}\sum_{i=1}^{N_{\rm eve}} \frac{t_{\rm E,i}}{\epsilon\,(t_{\rm E,i})}$ represents the detection-efficiency-corrected total effective $t_{\rm in}$ for all sources, denoted as $t_{\rm in,total}$. Thus, Equation (8) can be understood as expressing τ as the ratio of $t_{\rm in,total}$ to the survey duration $T_{\rm o}$, averaged over all monitored sources. This interpretation aligns directly with the observational expression of the microlensing optical depth as the average fraction of time that sources are within the Einstein radius during the survey.

The microlensing event rate, Γ, quantifies the frequency of microlensing events per source star per unit time and can observationally be derived as:

$$\Gamma = \frac{1}{N_{\rm s} T_{\rm o}} \sum_{i=1}^{N_{\rm eve}} \frac{1}{\epsilon\,(t_{\rm E,i})}. \tag{9}$$

This equation expresses Γ as the effective number of microlensing events, $N_{\rm eve,eff}$, normalized by the total number of source stars $N_{\rm s}$ and the duration of the survey $T_{\rm o}$. Here, $N_{\rm eve,eff}$ is the sum of efficiency-corrected contributions from each event, given by

$$N_{\rm eve,eff} = \sum_{i=1}^{N_{\rm eve}} \frac{1}{\epsilon\,(t_{\rm E,i})}. \tag{10}$$

This correction accounts for the fact that not all events are detected due to observational limitations, such as sensitivity to certain event timescales or background noise.

Equation (9) can be interpreted as the average rate of microlensing events observed per star in the surveyed population. Each event is weighted by $1/\epsilon(t_{\rm E,i})$, which compensates for the probability of missing events with a given Einstein radius crossing time $t_{\rm E,i}$. Events with lower detection efficiency contribute more significantly to $N_{\rm eve,eff}$, ensuring that Γ accurately reflects the true event rate.

Thus, this formulation connects the observed microlensing events, adjusted for detection efficiency, to the underlying astrophysical event rate. It encapsulates the idea that Γ represents the fraction of source stars that undergo microlensing per unit time, averaged across the surveyed population. This interpretation aligns closely with the observationally derived event rate while incorporating necessary efficiency corrections to mitigate biases in the raw data.

3. Data

The data set used in this analysis is the same one used in T. Sumi et al. (2023). This was taken during the 2006–2014 seasons of the MOA-II high cadence photometric survey toward the GB. MOA-II uses the 1.8 m MOA-II telescope located at the University of Canterbury's Mount John Observatory in New Zealand. The telescope is equipped with a wide field camera, MOA-cam3 (T. Sako et al. 2008), which consists of 10 2k × 4k pixel CCDs with 15 μm pixels. With the pixel scale of $0\farcs58$ pixel^{-1}, this gives a 2.18 deg^2 field of view. The median seeing for this data set is $2\farcs0$. The coordinates of the center of 20 MOA-II fields and the cadences are listed in Table 1. Note that gb6 and gb22, and some subfields in other fields, in all about 12% of the total survey area, are not used in our analysis because an RCG population could not be identified clearly in the CMD. Each field is divided into 80 subfields in which the photometric scale is individually calibrated in each subfield. The numbers of subfields for each field are also given

in Table 1. The total duration of the data set is 3146 days, spanning the period from HJD = 2453824 to HJD = 2456970. Data analysis and microlensing event selection for this data set were conducted by N. Koshimoto et al. (2023), which is a companion paper of T. Sumi et al. (2023). Here, we briefly introduce their process, but for more details, see N. Koshimoto et al. (2023).

3.1. Data Analysis

The observed images were reduced with the MOA implementation (I. A. Bond et al. 2001) of the difference image analysis (DIA) method (A. B. Tomaney & A. P. S. Crotts 1996; C. Alard & R. H. Lupton 1998; C. Alard 2000). This makes it possible to perform precise photometry even in very crowded fields such as the GB. Each field consists of 10 chips and each chip is divided into eight 1024 × 1024 pixel subfields during the DIA process. All photometric light curves were detrended by fitting a polynomial model given by Equation (4) of N. Koshimoto et al. (2023) to correct systematic trends correlated with seeing and airmass. The DIA light curve photometry values are given as flux values which are scaled to the MOA reference images. Calibration for MOA reference images was performed by cross-referencing the MOA-II DOPHOT catalog to the OGLE-III photometry map of the GB (M. K. Szymański et al. 2011).

3.2. Microlensing Event Selection

First, N. Koshimoto et al. (2023) detected variable objects on the subtracted images by using a custom implementation of the IRAF task DAOFIND (P. B. Stetson 1987) with the modification that both positive and negative point-spread function (PSF) profiles are searched for simultaneously. They eliminated the detection of spurious variations among all detected variable objects using the criteria listed in Table 2 of N. Koshimoto et al. (2023). As a result, 2,409,061 variable objects were detected at this stage of the analysis.

Second, they created the light curves of variable objects by using PSF-fitting photometry on the difference images. By imposing criteria on the number of data points and the signal-to-noise ratio of the light curve, 67,242 light curves were selected and 6111 microlensing candidates were found during this process.

Finally, they selected high-quality single-lens events based on the uncertainty of Einstein radius crossing times, the number of data points in the peak, and the residual from the best-fit model, etc. As a result, 3554 and 3535 objects remained as microlensing candidates after applying nominal criteria (CR1) and stricter criteria (CR2), respectively, among all visually identified 6111 candidates. All criteria are summarized in Table 2 of N. Koshimoto et al. (2023). In our analysis, we use only a sample from CR2, but in addition to the CR2 cut, we remove events with $t_{\rm E} \leqslant 1$ day because such short-timescale events are regarded as free-floating planet candidates which are not considered in predictions of microlensing optical depth and event rate from Galactic models.

Due to these selection criteria, all events with significant binary lens features were removed from the sample. To correct our optical depth measurement for binary lens events excluded from the sample, we assume that the fraction of binary lens events among all microlensing events is 6% (T. Sumi et al. 2013). As described in T. Sumi et al. (2013), this correction can be achieved by applying a factor of 1.09 to the optical depth and 1.06 to the event rate. The number of events in each field is listed in Table 1.

3.3. Detection Efficiency

For the calculation of detection efficiency, N. Koshimoto et al. (2023) performed image-level simulations of 6.4×10^7 artificial events. They generated 40,000 artificial events in each subfield and embedded them at random positions between $0 \leqslant x/\mathrm{pix} \leqslant 2048$ and $0 \leqslant y/\mathrm{pix} \leqslant 4096$ in each CCD. The microlensing parameters are randomly assigned between $3824 \leqslant t_0/\mathrm{JD}' \leqslant 6970$, $0 \leqslant u_0 \leqslant 1.5$, and a source magnitude of $14.2 \leqslant I_{\rm s}/\mathrm{mag} \leqslant 22$, uniformly. The detection efficiency was calculated as a function of Einstein radius crossing time, $t_{\rm E}$, and Einstein radius, $\theta_{\rm E}$, in each subfield.

We use the average detection efficiency of each field which is derived by integrating the detection efficiency of all subfields within that field weighted by $n_{{\rm RC},k}^2 f_{{\rm LF},k}(I_{{\rm s},i})$, where $n_{{\rm RC},k}$ is the number density of RCGs in the kth subfield, and $f_{{\rm LF},k}$ is the fraction of stars that have a source magnitude of ith artificial event, $I_{{\rm s},i}$, given by the luminosity function (LF) in the kth subfield (Equations (12), (13) of N. Koshimoto et al. 2023).

In our analysis, we use the one-dimensional detection efficiency as a function of $t_{\rm E}$ (see Equations (8), (9)). This is calculated by integrating the 2D detection efficiency, $\epsilon(t_{\rm E}, \theta_{\rm E})$, over $\theta_{\rm E}$ weighted by the fraction of events with $\theta_{\rm E}$ among events with $t_{\rm E}$ in the model, $\Gamma(\theta_{\rm E}|t_{\rm E})$ (Equation (11) of N. Koshimoto et al. 2023). The integrated detection efficiency for each field is illustrated in Figure 4 of T. Sumi et al. (2023).

3.4. Star Counts

For source star counts, we use a method similar to that of T. Sumi & M. T. Penny (2016), but with some updates.

T. Sumi & M. T. Penny (2016) constructed a combined LF in Baade's window by using the MOA-II Dophot star catalog for bright stars and Hubble Space Telescope (HST) deep imaging (J. A. Holtzman et al. 1998) for faint stars down to $I = 24$ mag. On the other hand, in this work, we used the LF based on the OGLE-III photometry map (M. K. Szymański et al. 2011) for bright stars. Because the OGLE LF is more accurate and deeper than the MOA-II LF due to superior seeing, longer exposure times, and a finer CCD pixel scale, it can be accurately normalized and aligned by using magnitude ranges overlapping the brighter end of the HST LF. This improved the accuracy of the number count of the source stars. We used RCGs to calibrate and normalize this combined LF to the extinction and GB distance for each subfield because RCG stars serve as reliable standard candles (M. Kiraga et al. 1997; K. Z. Stanek et al. 2000), a number of which can be considered to be proportional to the number of source stars in each subfield. We estimated the I-band magnitude of the center of RC, $I_{\rm RC}$, and the number of RCG stars, $N_{\rm RC}$, by fitting the LF of the MOA's reference images in each subfield with Equation (4) of D. M. Nataf et al. (2013). T. Sumi & M. T. Penny (2016) investigated the completeness of $N_{\rm RC}$ in the MOA-II GB fields by comparing it with that of OGLE-III (D. M. Nataf et al. 2013), and found that the ratio of $N_{\rm RC}$ between MOA-II and OGLE-III, $f_{\rm RC}$, is well expressed by $f_{\rm RC} = (0.63 \pm 0.01) - (0.052 \pm 0.003) \times b$ (Equation (2) of T. Sumi & M. T. Penny 2016). The $N_{\rm RC}$ is counted solely on the reference images and it is independent of the duration of the data set. The relationship derived in T. Sumi & M. T. Penny (2016)

remains applicable in this study because the same reference images are used in this work. We assume that the $N_{\rm RC}$ of OGLE-III is complete and correct the incompleteness of our $N_{\rm RC}$ using this linear relationship. We calculate the number of source stars, $N_{\rm s}$, by integrating this scaled-combined LF over the specified magnitude range (i.e., $10 \leqslant I_{\rm s} \leqslant 21.4$).

We also made two other updates in the calibration of the LF. As we mentioned above, we used $I_{\rm RC}$ and $N_{\rm RC}$ for calibrating the LF. We derived $I_{\rm RC}$ and $N_{\rm RC}$ by fitting the magnitude distribution of the reference images in each subfield with Equation (4) of D. M. Nataf et al. (2013). T. Sumi & M. T. Penny (2016) ignored the term related to the asymptotic giant branch bump in Equation (4) of D. M. Nataf et al. (2013). Since this omission may have introduced systematic errors in the calculation of $I_{\rm RC}$ and $N_{\rm RC}$, in this work, we incorporated this term into the calculation. We also updated the calibration of the photometric zero-point from instrumental magnitudes of the MOA reference images to the Kron/Cousins I band, which is also important for calibrating the LF. T. Sumi & M. T. Penny (2016) estimated the mean magnitude zero-point from the 30% of MOA-II fields that overlap with the OGLE-II map and applied this mean zero-point to all of the fields. This approach, however, introduced an uncertainty of approximately 0.25 mag in the calibration of each subfield. Thus, we instead use the OGLE-III photometry map to calibrate for each subfield individually, which provides more precise calibration. These updates improved the accuracy of the source star counts in this study.

As a result of these updates, our source star counts are a factor of 1.5 larger than the previous source star counts by T. Sumi & M. T. Penny (2016) as described in Section 5.1. In addition, we compared the number densities of stars brighter than $I = 21$ mag calculated by this updated method with those from P. Mróz et al. (2019) in each subfield and found that they are consistent within a factor of $1.06^{+0.39}_{-0.25}$(=MOA/OGLE).

4. Results

In this section, we estimated the optical depth and the event rate by following T. Sumi et al. (2013) and T. Sumi & M. T. Penny (2016). We calculated the optical depth, τ, the event rate per star per year, Γ, and the event rate per square degree per year, $\Gamma_{\rm deg^2}$, in each subfield by using Equations (8) and (9) and show the results in Figure 1(a). In addition, the mean Einstein radius crossing time weighted by detection efficiency ($=N^{-1}_{\rm eve,eff}\sum_{i=1}^{N_{\rm eve}} t_{\rm E,i}/\epsilon(t_{\rm E,i})$) is also presented. In panel (b), we also present the color maps of predictions from `genulens`, as described in Section 5. Note that all maps are smoothed with a Gaussian with $\sigma = 24'$ within 1° around the subfield. The combined average optical depth and event rate in each field are listed in Table 1. Uncertainties in the event rates are calculated by Poisson statistics, but a calculation of uncertainty in the optical depth is more complicated because it does not follow Poisson statistics. To estimate the uncertainty in the optical depth, we follow the bootstrap Monte Carlo method described in T. Sumi et al. (2013) and Section 6.1 of C. Alcock et al. (1997). Regarding the mean Einstein radius crossing time, $\langle t_{\rm E}\rangle$, we present the standard errors of the mean.

We estimated the average optical depth in all fields combined as $\tau = (1.61 \pm 0.04) \times 10^{-6}$. This is ∼5% higher than the result of $\tau = 1.53^{+0.12}_{-0.11} \times 10^{-6}$ based on the first two years of the MOA-II survey (T. Sumi & M. T. Penny 2016), but note that their result is based on source stars with $I < 20$ whereas ours is based on source stars with $I < 21.4$. A comparison in the same magnitude range is made in Section 5.1. The measured optical depth and event rate of the central region with $l < 5°$ is shown in Table 2. This is binned with a bin width of $\Delta b = 30'$ between $-6.^{\circ}5 < b < -1°$.

4.1. Fitting the Optical Depth with Parametric Model

In this section, we present a fitting with a parametric model to the result of the optical depth in Table 2. To estimate the Probability Density Function (PDF) of the measured optical depth in each bin, we resample N events from the sample within each bin, where N is drawn from a Poisson distribution with a parameter equal to the number of events in each bin. Assuming that the optical depth values computed in each subsample follow the PDF of measured optical depth, we estimate it by performing Kernel Density Estimation using that set of optical depth.

We adopted the simple exponential model given by $\tau = \tau_0 \exp[c_\tau(3° - |b|)]$ and found $\tau_0 = (1.75 \pm 0.04) \times 10^{-6}$ and $c_\tau = 0.34 \pm 0.02$ at $|l| < 5°$ by using the Markov Chain Monte Carlo (MCMC) method. The median and 99% confidence level of the MCMC results and data are shown in Figure 2(a).

4.2. Fitting the Event Rate with Parametric Model

Modeling the event rate is much simpler than that in the optical depth because the event rate follows Poisson statistics. From the definition of the event rate, the expected number of events, $N_{\rm exp}$, under an assumed model at coordinates (l, b), $\Gamma_{\rm model}(l, b)$, is given by

$$N_{\rm exp}(l, b; \Gamma_{\rm model}) = \Gamma_{\rm model}(l, b) N_{\rm s}(l, b) T_{\rm o} \langle \epsilon(l, b)\rangle, \quad (11)$$

where $N_{\rm s}(l, b)$ and $\langle\epsilon(l, b)\rangle$ are number of source stars and detection efficiency averaged over $t_{\rm E}$ weighted by $t_{\rm E}$ distribution at coordinates (l, b), respectively. For calculating the $t_{\rm E}$ distribution at coordinates (l, b), we use the Galactic model developed by N. Koshimoto et al. (2021) and their microlensing event simulation tool, `genulens`[17](N. Koshimoto & C. Ranc 2022). $N_{\rm s}^{\rm eff}(l, b) \equiv N_{\rm s}(l, b)\langle\epsilon(l, b)\rangle$ can be regarded as the effective number of source stars, taking into account the detection efficiency. We denote f as $\Gamma_{\rm model} T_{\rm o}$, which can be interpreted as the probability of a single star being microlensed during duration, $T_{\rm o}$. Under the effective number of stars, $N_{\rm s}^{\rm eff}$, and microlensed probability, f, the probability of the number of events, $N_{\rm eve}$, is given by

$$P[N_{\rm eve}] = \binom{N_{\rm s}^{\rm eff}}{N_{\rm eve}} f^{N_{\rm eve}} (1-f)^{N_{\rm s}^{\rm eff} - N_{\rm eve}} \times N_{\rm s}^{\rm eff} \to \infty \frac{(f N_{\rm s}^{\rm eff})^{N_{\rm eve}}}{N_{\rm eve}!} e^{-f N_{\rm s}^{\rm eff}}. \quad (12)$$

Note that the notations for (l, b) are omitted in this equation. Because $f(l, b) N_{\rm s}^{\rm eff}(l, b) = N_{\rm exp}(l, b)$ (Equation (11)), we can finally derive the expression for the likelihood as

$$\mathcal{L}[N_{\rm exp}(l, b; \Gamma_{\rm model}) | N_{\rm eve}(l, b)] = \frac{N_{\rm exp}(l, b)^{N_{\rm eve}(l,b)}}{N_{\rm eve}(l, b)!} e^{-N_{\rm exp}(l,b)}. \quad (13)$$

[17] https://github.com/nkoshimoto/genulens

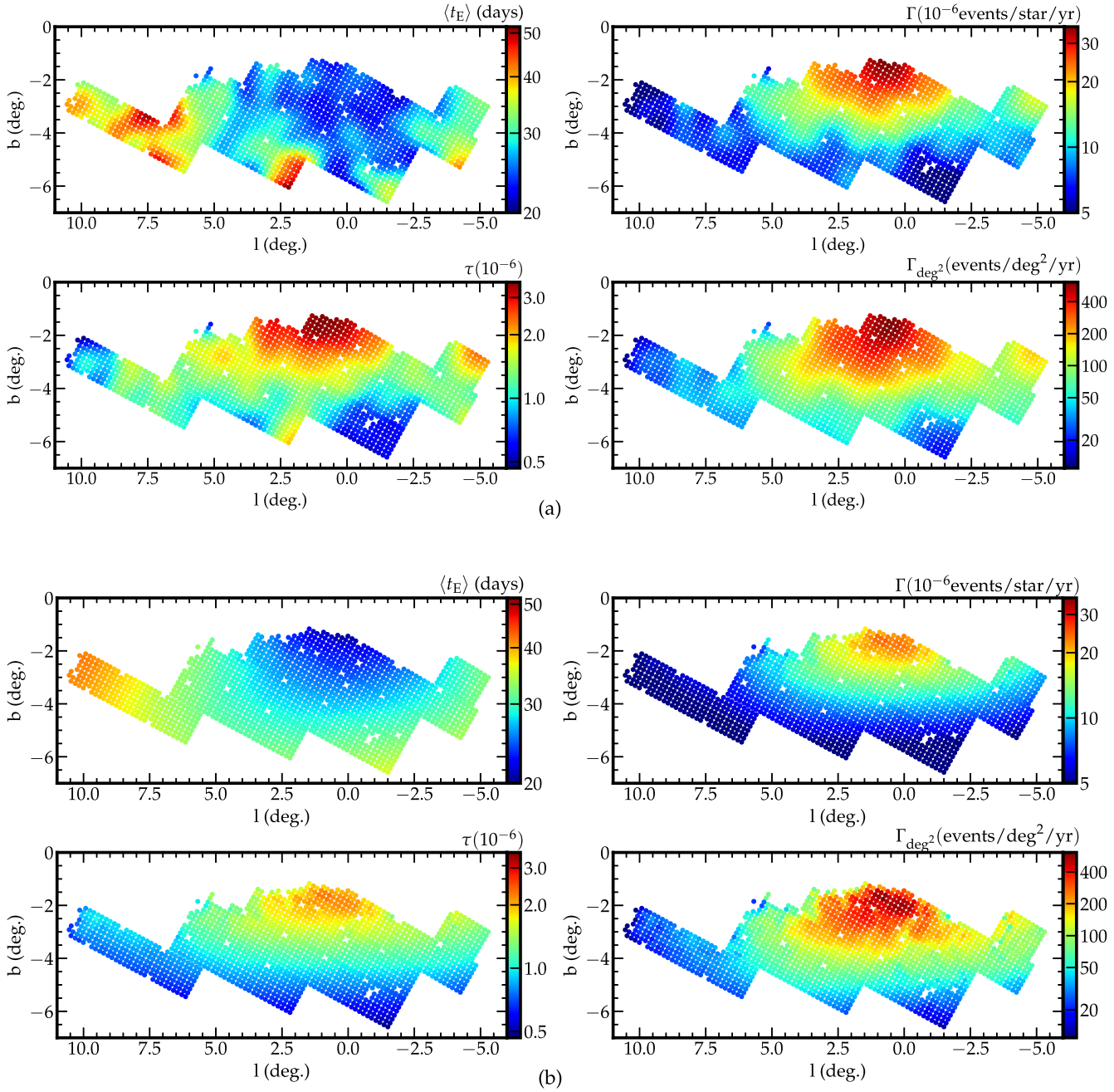

Figure 1. (a) Color map of the mean Einstein radius crossing time, $\langle t_E \rangle$, microlensing optical depth, τ, and event rate per star per year, Γ, based on the MOA-II microlensing survey (2006–2014). (b) Same as (a), but predictions by `genulens` (N. Koshimoto & C. Ranc 2022).

Under a uniform prior, a model can be evaluated by calculating $\prod_{(l,b)} \mathcal{L}[N_{\rm exp}(l, b; \Gamma_{\rm model})|N_{\rm eve}(l, b)]$.

As well as the case of optical depth, we adopt the simple exponential model given by $\Gamma = \Gamma_0 \exp[c_\Gamma(3^\circ - |b|)]$. Using the MCMC method, we estimated that $\Gamma_0 = (16.08 \pm 0.28) \times 10^{-6}$ and $c_\Gamma = 0.44 \pm 0.02$. The median and 99% confidence level of the MCMC result and the data are shown in Figure 2 (b).

5. Discussion

5.1. Comparison with Previous Results

P. Mróz et al. (2019) compared their measurement of the optical depth, τ, and event rate, Γ, based on the data from 8 yr of OGLE-IV observation with the result from the MOA-II 2 yr survey (T. Sumi & M. T. Penny 2016). As a result, they found that τ and Γ from OGLE-IV are factors of $\sim$1.4 lower than those based on the MOA-II all source events. We compare our new measurements from the MOA-II 9 yr data with those previous results.

Because T. Sumi & M. T. Penny (2016) use only events with $I_s < 20$ mag and $t_E < 200$ days, we follow suit and re-selected only events that satisfy the same criteria in our sample of 3525 events. As a result of this cut, a total of 2436 events remained in our sample. We also re-calculate detection efficiencies using only samples with $I_s < 20$ mag in the image-level simulation described in Section 3.3.

We fit the optical depth and event rate of the central region with $|l| < 3^\circ$ for the reselected 2436 sample using the same

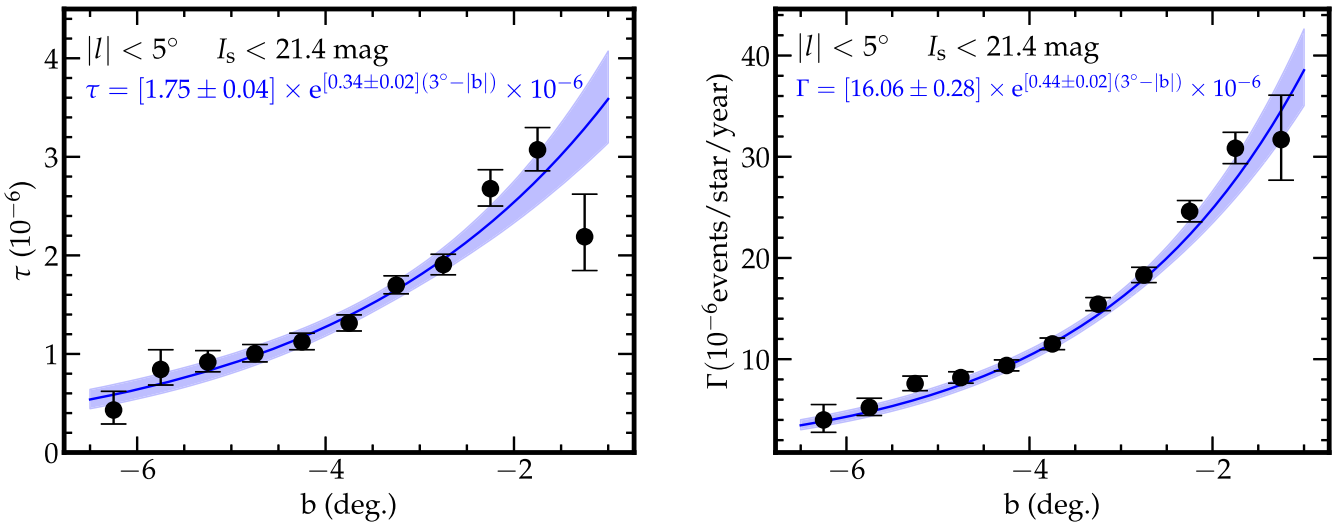

Figure 2. (a) Measured optical depths and (b) measured event rates for sources with $I_s < 21.4$ as a function of Galactic latitude b, within $|l| < 5^\circ$ (optical depths) and $|l| < 3^\circ$ (event rates), binned with a width of 30′ . The solid lines and shaded area indicate the median and 99% confidence level of the MCMC results, respectively. Data values for both quantities are listed in Table 2.

Table 2
The Microlensing Optical Depth and Event Rate for Source with $I < 21.4$ in b within $|l| < 5^\circ$

$\langle b \rangle$ (°)	N_{sub}	N_s	N_{eve}	τ (10^{-6})	Γ (10^{-6} star^{-1} yr^{-1})	Γ_{deg^2} (deg^{-2} yr^{-1})
−1.4012	20	4595283	57	$2.19^{+0.43}_{-0.34}$	$31.70^{+4.38}_{-4.02}$	$267.25^{+36.95}_{-33.86}$
−1.7690	70	25837259	395	$3.07^{+0.23}_{-0.21}$	$30.84^{+1.57}_{-1.52}$	$417.74^{+21.27}_{-20.57}$
−2.2645	114	38087885	540	$2.68^{+0.19}_{-0.18}$	$24.61^{+1.07}_{-1.04}$	$301.70^{+13.10}_{-12.73}$
−2.7576	146	50452070	585	$1.91^{+0.11}_{-0.10}$	$18.31^{+0.76}_{-0.74}$	$232.21^{+9.68}_{-9.42}$
−3.2486	168	54692934	567	$1.70^{+0.10}_{-0.09}$	$15.43^{+0.65}_{-0.64}$	$184.39^{+7.81}_{-7.60}$
−3.7490	172	49078606	400	$1.31^{+0.08}_{-0.08}$	$11.51^{+0.58}_{-0.56}$	$120.50^{+6.10}_{-5.90}$
−4.2512	172	42129953	295	$1.12^{+0.09}_{-0.08}$	$9.38^{+0.55}_{-0.53}$	$84.29^{+4.98}_{-4.79}$
−4.7410	154	32367770	206	$1.00^{+0.09}_{-0.08}$	$8.18^{+0.58}_{-0.55}$	$63.09^{+4.48}_{-4.28}$
−5.2270	101	18008997	111	$0.92^{+0.12}_{-0.10}$	$7.59^{+0.74}_{-0.70}$	$49.65^{+4.85}_{-4.55}$
−5.7197	56	8310438	38	$0.84^{+0.20}_{-0.16}$	$5.24^{+0.90}_{-0.81}$	$28.54^{+4.89}_{-4.40}$
−6.1945	19	2428901	9	$0.43^{+0.19}_{-0.14}$	$4.00^{+1.52}_{-1.23}$	$18.76^{+7.13}_{-5.76}$

Note. $\langle b \rangle$, N_{sub}, N_s, and N_{eve} indicate the average Galactic latitude, number of subfields, number of source stars, and number of microlensing events, respectively.

method described in Sections 4.1 and 4.2, and estimate that $\tau = [1.40 \pm 0.04]\exp[(0.36 \pm 0.03)(3^\circ - |b|)] \times 10^{-6}$ and $\Gamma = [14.18 \pm 0.30]\exp[(0.42 \pm 0.02)(3^\circ - |b|)] \times 10^{-6}$. Figures 3(a) and (b) present the data and best-fit models from the MOA-II 9 yr sample (this work), the MOA-II 2 yr sample (T. Sumi & M. T. Penny 2016), and the OGLE-IV 8 yr sample (P. Mróz et al. 2019). Our measurements of τ and Γ are systematically lower than the result from MOA-II 2 yr: $\tau = [1.84 \pm 0.14]\exp[(0.44 \pm 0.07)(3^\circ - |b|)] \times 10^{-6}$ and $\Gamma = [18.74 \pm 0.91]\exp[(0.53 \pm 0.05)(3^\circ - |b|)] \times 10^{-6}$ (T. Sumi & M. T. Penny 2016) and in agreement with result from OGLE-IV 8 yr: $\tau = [1.36 \pm 0.04]\exp[(0.39 \pm 0.03)(3^\circ - |b|)] \times 10^{-6}$ and $\Gamma = [13.4 \pm 0.3]\exp[(0.49 \pm 0.02)(3^\circ - |b|)] \times 10^{-6}$ (P. Mróz et al. 2019).

P. Mróz et al. (2019) attribute the relatively high optical depth and event rate measurement from MOA-II 2 yr to the incompleteness of source star counts. Indeed, they found that their star counts were a factor of 1.5 larger than those reported by T. Sumi & M. T. Penny (2016). Figure 4 compares the surface density of the source stars used in this study with those in T. Sumi & M. T. Penny (2016). We found that our star counts are a factor of 1.5 larger than those reported by T. Sumi & M. T. Penny (2016), which confirmed the findings of P. Mróz et al. (2019). This is due to the improvements in the source star counts method described in Section 3.4. The systematic difference in star counts is sufficient to explain the systematic excess in the measurements of τ and Γ by T. Sumi & M. T. Penny (2016). In fact, the event rate per square degree per year, Γ_{deg}^2, which is independent of the number of source stars, is roughly consistent with the results of T. Sumi & M. T. Penny (2016). Therefore, we conclude that the differences in the measurements of τ and Γ are due to the differences in source star counts. These systematics have been corrected in this work.

5.2. Comparison with Galactic Models

We compare our measurement of the optical depth, event rate, and the mean Einstein radius crossing time with values

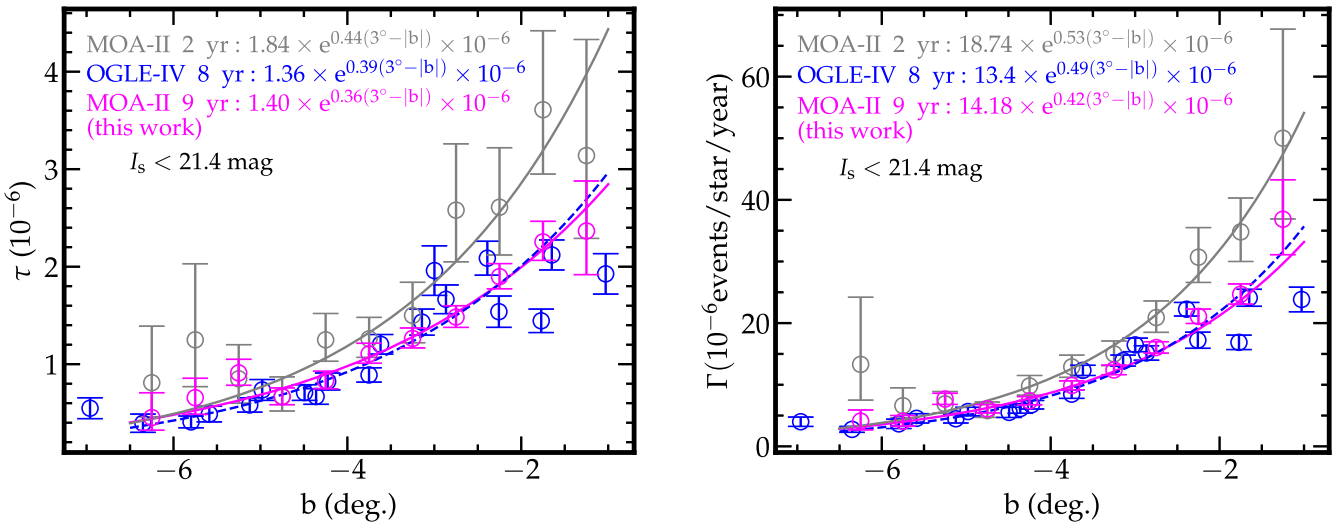

Figure 3. Microlensing (a) optical depths and (b) event rates for the central region ($|l| < 3°$) are compared between MOA-II 9 yr (this work), MOA-II 2 yr (T. Sumi & M. T. Penny 2016), and OGLE-IV 8 yr (P. Mróz et al. 2019). These measurements are based on events with $I_s < 20$ mag and $t_E < 200$ days. The gray, blue, and magenta circles represent the measurements from MOA-II 2 yr, OGLE-IV 8 yr, and MOA-II 9 yr, respectively, with the corresponding solid lines in each color indicating the best-fit models for these data sets.

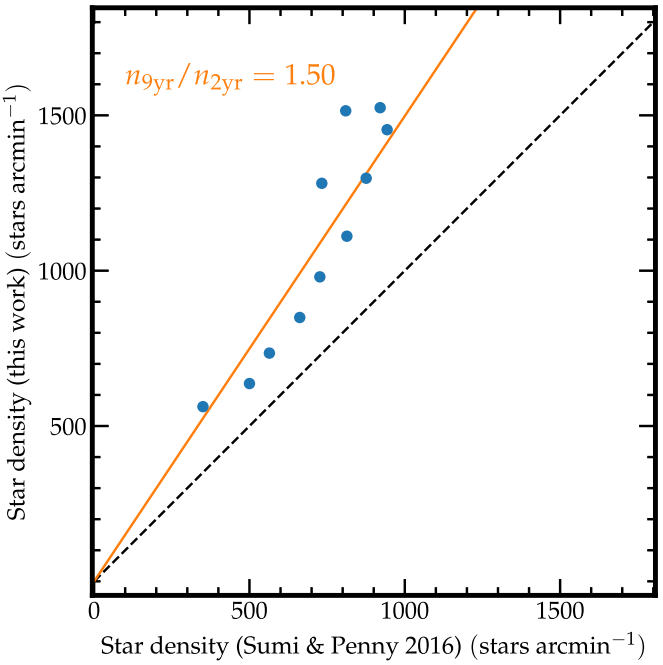

Figure 4. A comparison of the surface star density for the central region with $|l| < 3°$ between the data set used in T. Sumi & M. T. Penny (2016) and this study. Subfields are binned with a bin width of $\Delta b = 30'$.

predicted by models. For this comparison, we employ two microlensing simulators: the second-generation Manchester–Besançon Microlensing Simulator (MaBμlS-2[18]) from D. Specht et al. (2020) and a modified version of `genulens` (N. Koshimoto & C. Ranc 2022).

MaBμlS-2 is based on the Besançon Galactic synthesis model (A. C. Robin et al. 2014) and provides high-resolution microlensing maps of optical depth (τ), event rate per star per year (Γ), and average Einstein radius crossing timescales ($\langle t_E \rangle$) across a 400 deg^2 region of the GB. This model incorporates several critical improvements compared to its previous version, MaBμlS-1, including the treatment of unresolved stellar backgrounds, the use of limb-darkened source profiles, and more detailed corrections for extinction and star counts. The first field-by-field comparison between the Besançon model predictions and observational results was conducted by S. Awiphan et al. (2016), who compared τ and Γ from the MOA-II 2 yr data set (T. Sumi et al. 2013) with MaBμlS-1. Their analysis revealed that τ and Γ measured at low Galactic latitude ($|l| < 3°$) were approximately 50% higher than the predictions, likely due to underestimated extinction and star counts in the central regions.

Subsequently, T. Sumi & M. T. Penny (2016) addressed this discrepancy by correcting for the incompleteness in RCG counts used for normalizing the LF, resulting in revised estimates of τ and Γ. After these corrections, T. Sumi & M. T. Penny (2016) found reasonable agreement between the MOA-II results and the MaBμlS-1 predictions by S. Awiphan et al. (2016).

The second model we use for comparison is a modified version of `genulens` (N. Koshimoto & C. Ranc 2022), which is a microlensing event simulation tool based on the Galactic model developed by N. Koshimoto et al. (2021). This model was designed to reproduce the stellar distribution toward the GB by fitting to the Gaia DR2 velocity data (Gaia Collaboration et al. 2018), OGLE-III red clump star count data (D. M. Nataf et al. 2013), VIRAC proper motion catalog (L. C. Smith et al. 2018; J. P. Clarke et al. 2019), BRAVA radial velocity measurements (R. M. Rich et al. 2007; A. Kunder et al. 2012), and OGLE-IV star count and microlensing rate data (P. Mróz et al. 2017, 2019). Recently, K. Nunota et al. (2024) confirmed that this model can almost perfectly reproduce the two-dimensional distribution of t_E and μ_{rel} from the MOA-II 9 yr FSPL data set (N. Koshimoto et al. 2023). The color maps of predictions from `genulens` are presented in Figure 1(b).

[18] http://www.mabuls.net/

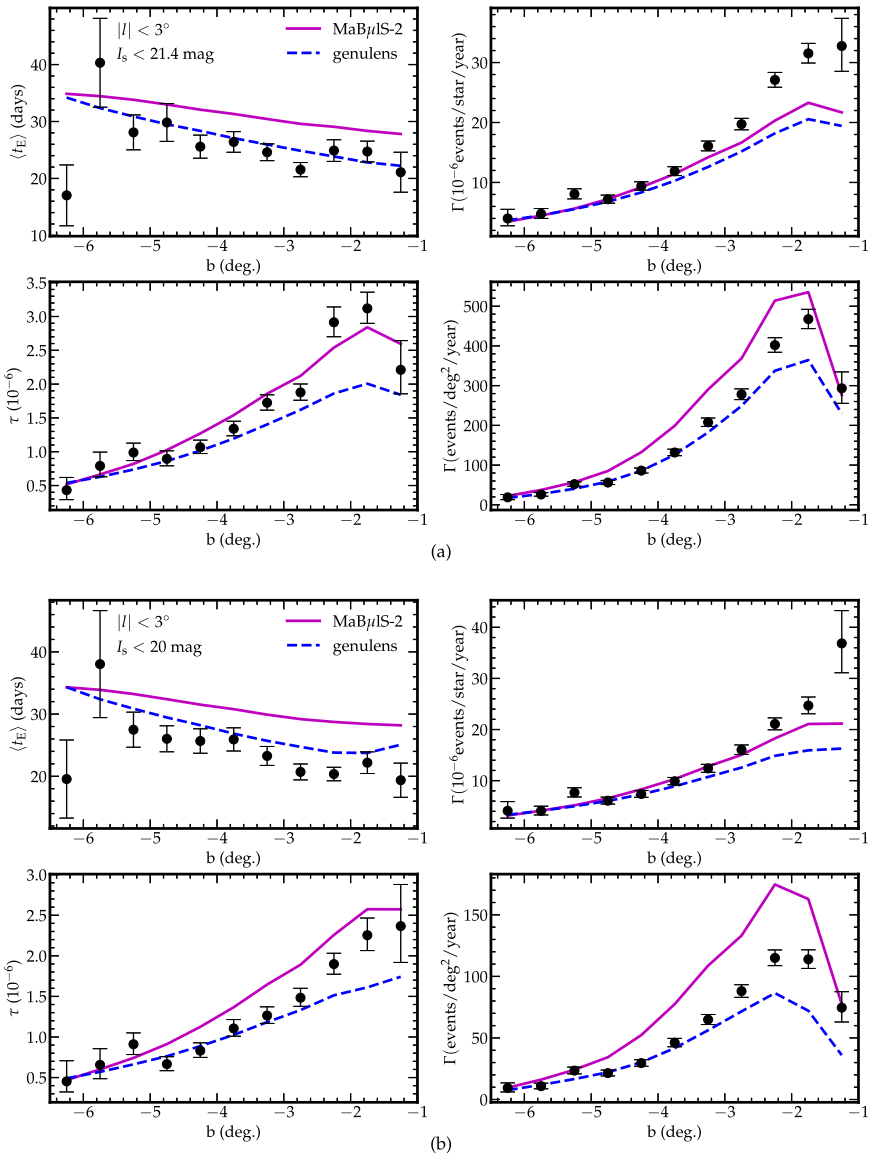

Figure 5. Comparison of the microlensing (a) optical depth, event rate, and mean Einstein radius crossing time for $I < 21.4$ mag and (b) for $I < 20$ mag in the central region ($l < 3°$). The purple solid line shows the prediction based on MaBμlS-2 (D. Specht et al. 2020), and the blue dotted line shows the prediction based on the modified version of `genulens` (N. Koshimoto & C. Ranc 2022).

Figures 5(a) and (b) compare the optical depth, event rate, and the mean Einstein radius crossing time predicted by two models with our measurement with $I < 21.4$ mag and $I < 20$ mag, respectively. Comparison of the models and data in both samples—$I < 21.4$ mag and $I < 20$ mag—are consistent and do not vary significantly between these two cases.

Regarding the mean Einstein radius crossing time, $\langle t_{\rm E} \rangle$, MaB$\mu$lS-2 systematically predicts higher values compared to the data, whereas `genulens` provides predictions that are in good agreement with our measurements. The systematic overestimation of the Einstein radius crossing time in the MaBμlS-2 is similarly mentioned in D. Specht et al. (2020).

On the other hand, neither model adequately explains the measured optical depth. There is a systematic excess in the data compared to the predictions from `genulens` in the central region with $|b| < 3°$, whereas the model performs well for $|b| > 3°$. MaBμlS-2 systematically predicts slightly higher values for $|b| > 3°$ but shows better predictions compared to `genulens` for $|b| < 3°$.

In contrast to the differing predictions for the mean Einstein radius crossing time and optical depth, both models predict nearly the same values for the event rate per star per year. These predictions are consistent with our observation for $|b| > 3°$, but they fail to reproduce the higher observed values in the central region with $|b| < 3°$. This systematic excess is also mentioned in D. Specht et al. (2020). Although both models show systematic differences from the data, MaBμlS-2 provides slightly better predictions compared to `genulens` for the event rate per star per year.

Regarding the event rate per square degree per year, the two models exhibit opposing behaviors relative to the data. While MaBμlS-2 tends to slightly overestimate the event rate, `genulens` shows a tendency to slightly underestimate it. This tendency is more pronounced in the central region $|b| < 3°$, and in fact, for $|b| > 3°$, `genulens` provides good predictions.

The MOA-II 9 yr survey data and the OGLE-IV survey data both report optical depths and event rates that align closely

despite being derived independently, confirming the consistency between the results of this study and those of P. Mróz et al. (2019). Furthermore, P. Mróz et al. (2019) noted that their findings are well matched with predictions from MaBμlS-1 (S. Awiphan et al. 2016). However, a significant inconsistency arises when comparing this study's results with predictions from the updated MaBμlS-2 model (D. Specht et al. 2020), particularly within the inner Galactic region ($|l| < 3°$). While MaBμlS-2 incorporates numerous improvements over its predecessor, D. Specht et al. (2020) reported that the normalized residuals for τ showed no improvement compared to MaBμlS-1. Furthermore, the new model exhibited a notable underprediction in the event rate per square degree outside the GB, which contrasts with the strong overprediction observed across the entire OGLE-IV rate map with MaBμlS-1.

D. Specht et al. (2020) proposed two potential reasons for these discrepancies. First, the stellar initial mass function and, by extension, the associated LFs might not accurately represent the true stellar populations, leading to a smaller predicted population of resolved stars. Second, the source weighting applied in the simulation might be insufficiently faithful to the observational data set, resulting in incorrect contributions from individual source stars. These issues may explain why MaBμlS-2, despite its advances, struggles to reconcile certain features of the OGLE-IV and MOA-II data sets.

6. Summary

We measured the microlensing optical depth, τ, and event rate, Γ, toward the GB using the data set from the MOA-II survey from 2006 to 2014. Our sample consists of 3525 microlens events, with an Einstein radius crossing time of 1 day $< t_E <$ 760 days. Our result is $\tau = [1.75 \pm 0.04]\exp[(0.34 \pm 0.02)(3° - |b|)] \times 10^{-6}$ and $\Gamma = [16.08 \pm 0.28]\exp[(0.44 \pm 0.02)(3° - |b|)] \times 10^{-6}$ in the central region with $|l| < 5°$.

These results are consistent with the latest OGLE-IV 8 yr data set (P. Mróz et al. 2019). We confirmed that the factor of $\sim$1.4 higher optical depth and event rate of the MOA-II 2 yr result compared to the OGLE-IV 8 yr result is due to a factor of 1.5 underestimate of the source star counts in MOA-II 2 yr analysis.

We also compared our results with model predictions, MaBμlS-2 (D. Specht et al. 2020), and a modified version of `genulens` (N. Koshimoto & C. Ranc 2022). We found a systematic discrepancy between the two models and our observed values, especially in the central region with $|b| < 3°$. Both models may need to be updated based on this result.

Microlensing event samples in Galactic central regions are expected to increase with upcoming microlensing surveys. The PRime-focus Infrared Microlensing Experiment (PRIME) began their survey toward the GB and center in 2023 (I. Kondo et al. 2023; H. Yama et al. 2023). PRIME is expected to discover $\sim$3900 microlensing events per year within $|b| < 3°$ (I. Kondo et al. 2023). In addition, the Nancy Grace Roman Space Telescope is planned to launch in late 2026 (D. Spergel et al. 2015) and a total of $\sim$27,000 microlensing events with $|u_0| < 1$ are expected to be discovered (M. T. Penny et al. 2019). It is anticipated that we can improve this work, like 2D fitting to the event rate map, by using these larger and enhanced samples in the future.

Acknowledgments

K.N. was supported by Ono Scholarship Foundation for a public interest incorporated foundation. The work of N.K. was supported JSPS KAKENHI grant Nos. JP24K17089 and JP23KK0060. D.S. was supported by JSPS KAKENHI grant No. 19KK0082, 20H04754, JPJSCCA20210003 and 24H01811.

Appendix
Detailed Data Tables for Each Subfield

This appendix provides an example of the detailed data tables for the subfields analyzed in this study. Table 3 focuses on the gb1 subfields and presents key measurements and results as a demonstration of the machine-readable table format. The complete data for all subfields are available in machine-readable format in the electronic version of this paper.

Table 3

MOA-II Galactic Bulge Sub Fields with Galactic Coordinates (l, b), the Number of Source Stars with $I_s < 21.4$ mag (N_s), the Number of Microlensing Events (N_{eve}), the Microlensing Event Rate per Star per Year (Γ), the Microlensing Event Rate per Square Degree per Year (Γ_{deg^2}), the Optical Depth (τ), the Average Einstein Radius Crossing Time ($\langle t_E \rangle$) Average, and the Average Detection Efficiency ($\langle \epsilon \rangle$)

Field	l (°)	b (°)	N_s (10^5)	N_{eve}	τ (10^{-6})	Γ (10^{-6} star^{-1} yr^{-1})	Γ_{deg^2} (deg^{-2} yr^{-1})	$\langle t_E \rangle$ (days)	$\langle \epsilon \rangle$ (10^{-2})
gb1-1-0	−4.10	−2.28	2.29	2	$2.52^{+3.81}_{-1.26}$	$11.75^{+2.71}_{-2.36}$	$98.73^{+22.80}_{-19.83}$	48.46 ± 18.74	8.61
gb1-1-1	−4.02	−2.42	3.30	4	$2.32^{+1.67}_{-1.16}$	$14.35^{+2.44}_{-2.20}$	$173.91^{+29.60}_{-26.62}$	36.49 ± 2.22	8.59
gb1-1-2	−3.93	−2.56	1.67	0	…	…	…	…	8.57
gb1-1-3	−3.84	−2.71	2.15	1	$1.01^{+2.10}_{-0.07}$	$5.24^{+1.97}_{-1.60}$	$41.22^{+15.54}_{-12.57}$	43.70	8.56
gb1-1-5	−3.87	−2.34	2.01	1	$1.14^{+2.39}_{-0.11}$	$5.51^{+2.09}_{-1.69}$	$40.71^{+15.46}_{-12.49}$	46.93	8.55
gb1-1-6	−3.79	−2.48	1.38	0	…	…	…	…	8.53
gb1-1-7	−3.70	−2.62	2.61	2	$2.02^{+3.01}_{-0.97}$	$8.49^{+2.18}_{-1.87}$	$81.20^{+20.88}_{-17.91}$	53.70 ± 8.42	8.52
gb1-2-0	−4.40	−2.46	3.04	3	$1.66^{+1.71}_{-0.60}$	$17.08^{+2.77}_{-2.50}$	$190.37^{+30.88}_{-27.90}$	21.92 ± 9.26	8.69
gb1-2-1	−4.32	−2.60	3.42	3	$1.03^{+0.97}_{-0.37}$	$14.28^{+2.39}_{-2.16}$	$179.04^{+30.00}_{-27.03}$	16.30 ± 3.15	8.67
gb1-2-2	−4.23	−2.74	3.49	3	$1.34^{+1.40}_{-0.47}$	$14.05^{+2.35}_{-2.12}$	$179.72^{+30.06}_{-27.08}$	21.62 ± 8.14	8.65
gb1-2-3	−4.14	−2.89	3.18	4	$3.60^{+2.66}_{-1.73}$	$14.78^{+2.53}_{-2.27}$	$172.28^{+29.47}_{-26.49}$	55.07 ± 12.49	8.64
gb1-2-4	−4.26	−2.37	3.22	3	$1.58^{+1.57}_{-0.56}$	$12.36^{+2.31}_{-2.06}$	$146.04^{+27.29}_{-24.31}$	28.91 ± 6.31	8.65
gb1-2-5	−4.17	−2.51	3.47	5	$1.79^{+1.09}_{-0.72}$	$20.00^{+2.78}_{-2.55}$	$254.51^{+35.40}_{-32.43}$	20.29 ± 2.42	8.63
gb1-2-6	−4.08	−2.66	2.53	0	…	…	…	…	8.61
gb1-2-7	−4.00	−2.80	0.85	1	$1.10^{+2.35}_{-0.08}$	$17.31^{+5.60}_{-4.65}$	$53.75^{+17.41}_{-14.44}$	14.38	8.60
gb1-3-0	−4.70	−2.64	3.19	4	$2.76^{+1.95}_{-1.37}$	$15.19^{+2.56}_{-2.30}$	$177.64^{+29.89}_{-26.92}$	41.07 ± 6.37	8.76
gb1-3-1	−4.62	−2.78	3.21	6	$4.89^{+3.24}_{-1.68}$	$22.22^{+3.05}_{-2.79}$	$261.47^{+35.86}_{-32.88}$	49.77 ± 9.44	8.74
gb1-3-2	−4.53	−2.92	3.08	5	$2.45^{+1.86}_{-1.01}$	$23.79^{+3.22}_{-2.95}$	$268.57^{+36.32}_{-33.34}$	23.28 ± 5.38	8.73
gb1-3-3	−4.44	−3.07	3.09	2	$0.28^{+0.28}_{-0.14}$	$20.75^{+3.01}_{-2.75}$	$235.44^{+34.12}_{-31.15}$	3.09 ± 0.07	8.72
gb1-3-4	−4.56	−2.55	2.96	3	$3.37^{+3.30}_{-1.22}$	$11.41^{+2.33}_{-2.05}$	$124.05^{+25.31}_{-22.34}$	66.71 ± 13.60	8.73
gb1-3-5	−4.47	−2.69	3.24	2	$0.90^{+0.92}_{-0.45}$	$7.94^{+1.88}_{-1.63}$	$94.43^{+22.35}_{-19.37}$	25.72 ± 1.89	8.71
gb1-3-6	−4.39	−2.84	3.33	6	$2.68^{+1.36}_{-0.87}$	$24.26^{+3.11}_{-2.87}$	$296.75^{+38.08}_{-35.10}$	24.94 ± 3.30	8.69
gb1-3-7	−4.30	−2.98	3.13	2	$2.06^{+2.09}_{-0.99}$	$6.51^{+1.75}_{-1.49}$	$74.81^{+20.13}_{-17.16}$	71.58 ± 1.68	8.68

(This table is available in its entirety in machine-readable form in the online article.)

ORCID iDs

Kansuke Nunota https://orcid.org/0009-0005-3414-455X

References

Afonso, C., Albert, J. N., Alard, C., et al. 2003, A&A, 404, 145
Alard, C. 2000, A&AS, 144, 363
Alard, C., & Lupton, R. H. 1998, ApJ, 503, 325
Alcock, C., Allsman, R. A., Alves, D., et al. 1997, ApJ, 486, 697
Awiphan, S., Kerins, E., & Robin, A. C. 2016, MNRAS, 456, 1666
Batista, V., Gould, A., Dieters, S., et al. 2011, A&A, 529, A102
Bond, I. A., Abe, F., Dodd, R. J., et al. 2001, MNRAS, 327, 868
Clarke, J. P., Wegg, C., Gerhard, O., et al. 2019, MNRAS, 489, 3519
Griest, K., Alcock, C., Axelrod, T. S., et al. 1991, ApJL, 372, L79
Gaia Collaboration, Katz, D., Antoja, T., et al. 2018, A&A, 616, A11
Hamadache, C., Le Guillou, L., Tisserand, P., et al. 2006, A&A, 454, 185
Holtzman, J. A., Watson, A. M., Baum, W. A., et al. 1998, AJ, 115, 1946
Kim, S.-L., Lee, C.-U., Park, B.-G., et al. 2016, JKAS, 49, 37
Kiraga, M., Paczyński, B., & Stanek, K. Z. 1997, ApJ, 485, 611
Koshimoto, N., Baba, J., & Bennett, D. P. 2021, ApJ, 917, 78
Koshimoto, N., & Ranc, C. 2022, nkoshimoto/genulens: Release version v1.2, Zenodo, doi:10.5281/zenodo.4784948
Koshimoto, N., Sumi, T., Bennett, D. P., et al. 2023, AJ, 166, 107
Kondo, I., Sumi, T., Koshimoto, N., et al. 2023, AJ, 165, 254
Kunder, A., Koch, A., Rich, R. M., et al. 2012, AJ, 143, 57
Mróz, P., Udalski, A., Skowron, J., et al. 2017, Natur, 548, 183
Mróz, P., Udalski, A., Skowron, J., et al. 2019, ApJS, 244, 29
Nataf, D. M., Gould, A., Fouqué, P., et al. 2013, ApJ, 769, 88
Nunota, K., Koshimoto, N., Suzuki, D., et al. 2024, ApJ, 967, 77
Paczynski, B. 1986, ApJ, 304, 1
Paczynski, B. 1991, ApJL, 371, L63
Penny, M. T., Gaudi, B. S., Kerins, E., et al. 2019, ApJS, 241, 3
Popowski, P., Griest, K., Thomas, C. L., et al. 2005, ApJ, 631, 879
Robin, A. C., Reylé, C., Fliri, J., et al. 2014, A&A, 569, A13
Rich, R. M., Reitzel, D. B., Howard, C. D., et al. 2007, ApJL, 658, L29
Sako, T., Sekiguchi, T., Sasaki, M., et al. 2008, ExA, 22, 51
Smith, L. C., Lucas, P. W., Kurtev, R., et al. 2018, MNRAS, 474, 1826
Specht, D., Kerins, E., Awiphan, S., et al. 2020, MNRAS, 498, 2196
Spergel, D., Gehrels, N., Baltay, C., et al. 2015, arXiv:1503.03757
Stanek, K. Z., Kaluzny, J., Wysocka, A., et al. 2000, AcA, 50, 191
Stetson, P. B. 1987, PASP, 99, 191
Sumi, T., Abe, F., Bond, I. A., et al. 2003, ApJ, 591, 204
Sumi, T., Bennett, D. P., Bond, I. A., et al. 2013, ApJ, 778, 150
Sumi, T., Koshimoto, N., Bennett, D. P., et al. 2023, AJ, 166, 108
Sumi, T., & Penny, M. T. 2016, ApJ, 827, 139
Szymański, M. K., Udalski, A., Soszyński, I., et al. 2011, AcA, 61, 83
Tomaney, A. B., & Crotts, A. P. S. 1996, AJ, 112, 2872
Udalski, A., Szymanski, M., Stanek, K. Z., et al. 1994, AcA, 44, 165
Udalski, A., Szymański, M. K., & Szymański, G. 2015, AcA, 65, 1
Yama, H., Suzuki, D., Miyazaki, S., et al. 2023, JAI, 12, 2350004